Lawrence Berkeley National Laboratory
Recent Work

Title

The Use of Graphene and Its Derivatives for Liquid-Phase Transmission Electron Microscopy of Radiation-Sensitive Specimens.

Permalink

Authors

Cho, Hoduk
Jones, Matthew R
Nguyen, Son C
et al.

The Use of Graphene and Its Derivatives for Liquid-Phase Transmission Electron Microscopy of Radiation-Sensitive Specimens

Hoduk Cho,[†,‡] Matthew R. Jones,[†] Son C. Nguyen,[†,§] Matthew R. Hauwiller,[†,‡] Alex Zettl,[‡,⊥,∥] and A. Paul Alivisatos*[,†,‡,∥,#]

†Department of Chemistry, University of California, Berkeley, California 94720, United States
‡Materials Sciences Division, Lawrence Berkeley National Laboratory, Berkeley, California 94720, United States
§The Hamburg Centre for Ultrafast Imaging, University of Hamburg, Luruper Chaussee 149, 22761 Hamburg, Germany
⊥Department of Physics, University of California, Berkeley, California 94720, United States
∥Kavli Energy NanoScience Institute, Berkeley, California 94720, United States
#Department of Materials Science and Engineering, University of California, Berkeley, California 94720, United States

S Supporting Information

ABSTRACT: One of the key challenges facing liquid-phase transmission electron microscopy (TEM) of biological specimens has been the damaging effects of electron beam irradiation. The strongly ionizing electron beam is known to induce radiolysis of surrounding water molecules, leading to the formation of reactive radical species. In this study, we employ DNA-assembled Au nanoparticle superlattices (DNA-AuNP superlattices) as a model system to demonstrate that graphene and its derivatives can be used to mitigate electron beam-induced damage. We can image DNA-AuNP superlattices in their native saline environment when the liquid cell window material is graphene, but not when it is silicon nitride. In the latter case, initial dissociation of assembled AuNPs was followed by their random aggregation and etching. Using graphene-coated silicon nitride windows, we were able to replicate the observation of stable DNA-AuNP superlattices achieved with graphene liquid cells. We then carried out a correlative Raman spectroscopy and TEM study to compare the effect of electron beam irradiation on graphene with and without the presence of water and found that graphene reacts with the products of water radiolysis. We attribute the protective effect of graphene to its ability to efficiently scavenge reactive radical species, especially the hydroxyl radicals which are known to cause DNA strand breaks. We confirmed this by showing that stable DNA-AuNP assemblies can be imaged in silicon nitride liquid cells when graphene oxide and graphene quantum dots, which have also recently been reported as efficient radical scavengers, are added directly to the solution. We anticipate that our study will open up more opportunities for studying biological specimens using liquid-phase TEM with the use of graphene and its derivatives as biocompatible radical scavengers to alleviate the effects of radiation damage.
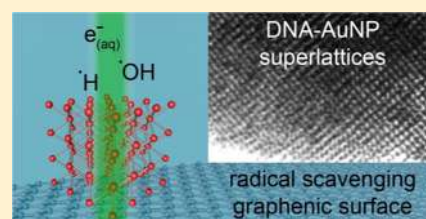
KEYWORDS: Liquid-phase TEM, graphene liquid cell, DNA nanotechnology, bioimaging, radical scavenger, radiation damage

Liquid-phase transmission electron microscopy (TEM) is a technique that allows direct real-time imaging of dynamic nanoscale processes occurring in solution. Advances in microfabrication led to the development of the first liquid cells that made use of thin silicon nitride membranes as electron transparent imaging windows.[1] In these silicon nitride liquid cells, a submicron layer of liquid is encapsulated between a pair of microchips to ensure compatibility with the high vacuum conditions inside an electron microscope. This method has subsequently been commercialized by several companies, greatly increasing the accessibility of the technique, and the current state of the art silicon nitride liquid cell technology allows for liquid flow as well as in situ heating and electrical biasing.[2] At first sight, the ability to directly visualize nanoscale matter in an aqueous environment should make it ideal for studying single particle dynamics of biological specimens, as long as the specimen in question is labeled with nanoparticles (NPs) for enhanced contrast. Direct imaging may also become

feasible if phase contrast enhancement approaches for TEM improve significantly. Although silicon nitride liquid cells have been used to image biological samples in hydrated environments,[3−6] their application to study biomolecules that are highly sensitive to radiation damage has been limited.[7−10] In addition to the direct ionization damage resulting from interactions between the energetic electrons and the specimen itself,[11] the electron beam also induces radiolysis of surrounding water molecules which in turn produces highly reactive species, including hydroxyl radicals, which are damaging to biological matter.[12−18]

Graphene liquid cells present an alternative to conventional silicon nitride liquid cells; liquid encapsulation is achieved using
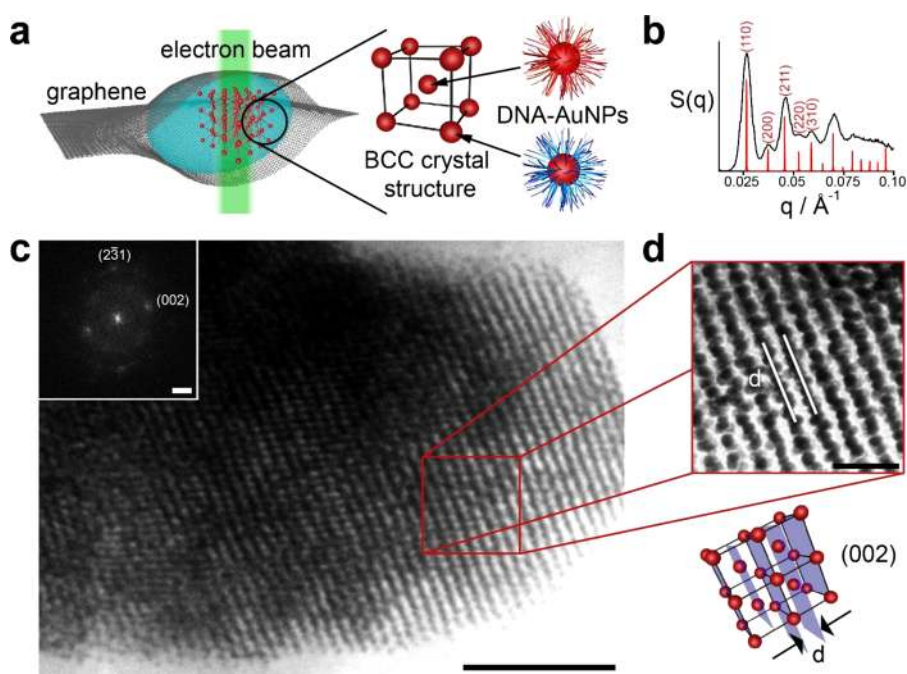
Figure 1. Liquid-phase TEM of stable DNA-AuNP superlattices in their native aqueous environment using graphene liquid cells. (a) Schematic illustration showing encapsulation of DNA-AuNP superlattices in aqueous solution using a graphene liquid cell. Two sets of DNA-AuNPs, functionalized with oligonucleotides that contain complementary sticky ends (represented by red and blue strands), assemble into a BCC crystal structure. (b) SAXS characterization of BCC DNA-AuNP superlattices in solution. The black and red traces are the experimentally obtained and the theoretical scattering patterns for a BCC crystal lattice, respectively. (c) A representative TEM image of DNA-AuNP superlattices taken using graphene liquid cell TEM. The scale bar is 200 nm. The inset shows the corresponding FFT image which matches the diffraction pattern of a BCC crystal with the [320] zone axis. The scale bar is 0.1 nm^{-1}. (d) Higher magnification TEM image showing the ordered arrangement of AuNPs. The lattice spacing corresponds to (002) planes in a BCC crystal structure. The scale bar is 50 nm.

impermeable graphene sheets, with the strong van der Waals interaction between adjacent graphene sheets driving the formation of liquid pockets.[19] Previous studies with bacteria,[20] small DNA-AuNP conjugates,[21,22] proteins,[23] viruses,[24] and cells[24] have shown that it is possible to image graphene-encapsulated hydrated biological samples for several minutes without visible structural damage. Apart from the empirically observed protection against radiation damage, graphene liquid cells also offer superior spatial resolution and contrast due to minimal electron scattering by the atomically thin graphene windows and the minuscule liquid pockets that can reach as low as several nanometers in height.[19] Nevertheless, there are intrinsic drawbacks to graphene liquid cells. Due to the inherently hermetic configuration of the liquid pockets and the uncontrolled nature of their formation, technical advances in microfluidics for silicon nitride liquid cells have not been easily transferable. Moreover, the success rate of liquid encapsulation has been found to depend heavily on the system under investigation. If we can elucidate the origin of the observed protective ability of graphene liquid cells, it is conceivable that we may be able to apply this mechanism to the silicon nitride liquid cell studies where radiation damage has been more problematic.

It has been speculated that graphene's excellent electrical and thermal conductivities may be responsible for reducing radiation damage to the encapsulated specimen, based on previous studies involving dry samples where local electrostatic charging and heating play important roles.[25−27] However, the extrapolation of such conclusions to explain the phenomena in liquid-phase TEM is not fully justified as they do not account for the considerable effects that reactive radical species are

known to have. Furthermore, there has not yet been a comparative study of the specimen stability in both graphene and silicon nitride liquid cells to examine the degree of protection. In this work, we utilize DNA-assembled AuNP superlattices (DNA-AuNP superlattices) in aqueous solution as a model system to compare the stability of DNA, which is known to be highly susceptible to radiation damage,[12−18] during liquid-phase TEM imaging in different liquid cell configurations. Lattice parameters and crystal symmetry of DNA-AuNP superlattices are dictated by the sequence-programmable DNA hybridization interactions between neighboring particles.[28−30] The direct observation and preservation of DNA-mediated long-range ordering of AuNPs, used here as high contrast markers, would demonstrate the structural stability of interparticle oligonucleotide linkages. Aside from the loss of global long-range order, structural damage could also manifest itself more locally in the form of DNA strand breaks,[12,14,17] which would result in dissociation of assembled AuNPs. Hence it is possible that the use of DNA-AuNP superlattices as a probe could provide more information about the liquid cell environment under irradiation than small DNA-AuNP conjugate systems.

We first used graphene liquid cells to image DNA-AuNP superlattices in their native aqueous solution of NaCl and phosphate buffer (Figure 1a). Body-centered cubic (BCC) DNA-AuNP superlattices were assembled from two sets of separately functionalized spherical 10 nm AuNPs, each containing DNA single-strand sticky ends that are non-self-complementary but complementary to the other type (Figure S1). The BCC arrangement is thermodynamically favored as this maximizes the number of nearest neighbors with
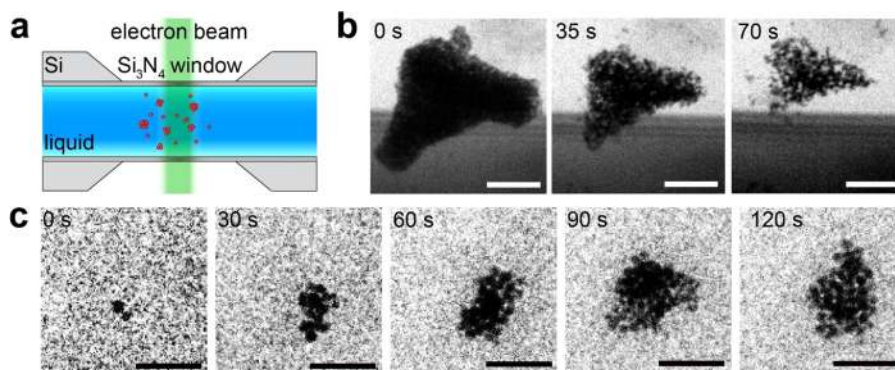
Figure 2. Destabilization of DNA linkages in DNA-AuNP superlattices and subsequent uncontrolled aggregation of dissociated particles when imaged using silicon nitride liquid cell TEM. (a) Experimental design of silicon nitride-based liquid cell TEM. (b) Time series of TEM images showing destabilization of oligonucleotide linkages in DNA-AuNP superlattices resulting in their dissociation into individual particles upon electron beam illumination. The scale bar is 200 nm. See Video S3 for the full movie. (c) Time series of TEM images after beam-induced destabilization of DNA-AuNP superlattices showing subsequent aggregation of individual AuNPs into close-packed structures without the expected interparticle spacing or long-range order. The scale bar is 50 nm. See Video S4 for the full movie.

complementary sticky ends.[28] Small-angle X-ray scattering (SAXS) was used to characterize the structure of prepared DNA-AuNP superlattices in solution, and the obtained scattering pattern shown in Figure 1b confirmed that ordering is BCC with the separation of 28.7 nm between the centers of two nearest neighboring AuNPs (see Supporting Information). Whereas face-centered cubic and hexagonal close-packed arrangements represent the densest packing of spheres of identical size and are known to form in the presence of non-specific interparticle forces,[31,32] a BCC arrangement generally does not form under thermodynamic conditions. Therefore, observation of BCC DNA-AuNP superlattices using liquid-phase TEM would be indicative of intact DNA hybridization-mediated assembly. Using graphene liquid cell TEM, we were able to image DNA-AuNP superlattices that exhibited long-range periodic ordering of AuNPs with clearly visible lattice spacings (Figure 1c). Analysis of the corresponding fast Fourier transform (FFT) image (the inset in Figure 1c) shows that the diffraction pattern belongs to that of a BCC crystal with the [320] zone axis. The lattice spacing between (002) planes is 16.5 nm, which is consistent with the value of 16.6 nm predicted from the SAXS data. Figure 1d shows a higher magnification image where individual AuNPs in the ordered array can be distinguished. Under typical imaging conditions, with electron dose rates ranging from 10 to 250 $e^-/(Å^2·s)$ depending on the magnification, DNA-AuNP superlattices did not undergo significant structural rearrangements for several minutes and appeared to be stable inside the liquid pockets. When the electron beam was focused, such that the electron dose rate was increased by approximately an order of magnitude, the periodic arrangement of AuNPs became disordered by convection due to vigorous bubble formation in the liquid pockets before drying out completely (Videos S1 and S2). Because BCC ordering of AuNPs is only possible through programmed DNA hybridization interactions, we can deduce that most of the oligonucleotide linkages present in DNA-AuNP superlattices retain their structural integrity during imaging. For the observed disordering of AuNPs at high electron beam intensities, it is difficult to decouple the effects of DNA damage from bubble-induced convection. In dry regions of graphene liquid cell samples where liquid was not successfully trapped, we only observed collapsed DNA-AuNP

assemblies without long-range order or the expected inter-particle spacing (Figures S2 and S3).

Our observation of DNA-AuNP superlattices that are structurally stable during imaging is consistent with previous graphene liquid cell TEM studies of DNA-AuNP dimers, trimers, and pyramids where AuNPs were connected to each other via single DNA duplexes.[21,22] Even so, this result is still surprising since the high vulnerability of hydrated DNA toward ionizing radiation is well-established.[12−18] Besides the direct ionization damage, electron beam-induced water radiolysis reactions give rise to the formation of highly reactive species, including hydrogen radicals, hydroxyl radicals, and hydrated electrons, that create an extremely hostile environment for biological systems.[12−18] In particular, hydroxyl radicals are responsible for most of the radiation damage to DNA molecules in solution as they can readily undergo hydrogen atom abstraction from deoxyribose or electrophilic addition to C=C and C=N π-bonds in nucleobases.[12−14,18] The chemical modification of nucleobases weakens the hydrogen bonding interaction,[14] while hydrogen abstraction from the sugar ring leads to cleavage of the sugar−phosphate backbone, resulting in DNA single-strand and double-strand breaks.[12,14,17] Although DNA cross-linking is also a known side effect of ionizing radiation, this is limited to intrastrand cross-linking, and thus it is unlikely that DNA-AuNP superlattices are held together during imaging via interstrand cross-linked DNA.[33,34] In fact, the dissociation of AuNPs in small DNA-AuNP conjugates after prolonged exposure or at increased beam intensities was reported in the previous studies.[21,22] Without any in situ protection mechanisms, it is expected that DNA-AuNP superlattices would disintegrate into individual AuNPs.

We next imaged DNA-AuNP superlattices using silicon nitride liquid cells under similar electron dose rates in order to directly compare the extent of radiation damage (Figure 2a). DNA-AuNP superlattices from the same stock solution containing NaCl and phosphate buffer were encapsulated between two microchips, each with a 50 nm thick silicon nitride window. The most striking observation was the extremely small number of DNA-AuNP superlattices that could be found in the viewing area compared to the graphene liquid cell. It has been reported that the silicon nitride surfaces can be negatively charged at pH values above 6 due to deprotonation of silanol and silylamine groups.[35] We speculate that the highly negatively
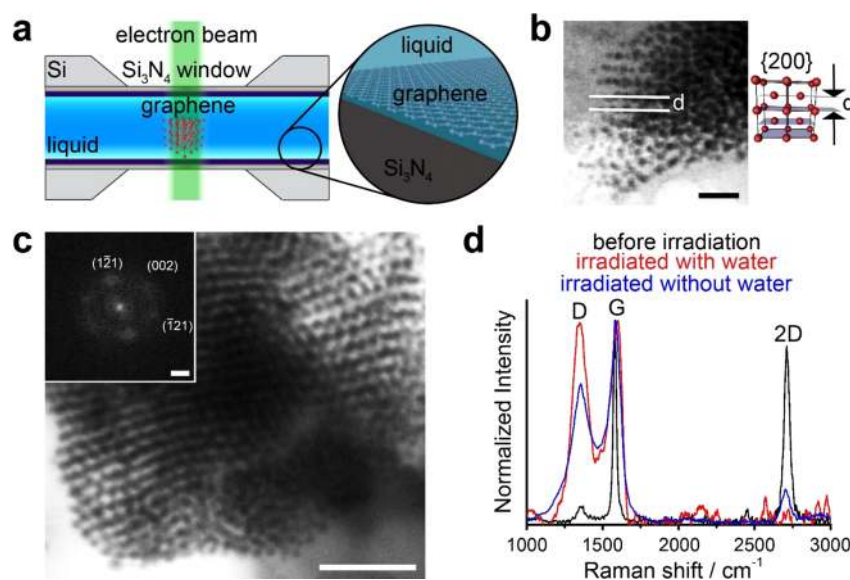
Figure 3. Imaging of DNA-AuNP superlattices in liquid using a graphene-coated silicon nitride liquid cell. (a) Experimental setup of graphene-coated silicon nitride liquid cell TEM. (b) TEM snapshot of DNA-AuNP superlattices. The lattice spacing indicated corresponds to the {200} planes in a BCC crystal structure. The scale bar is 50 nm. See Video S5 for the full movie. (c) TEM snapshot of DNA-AuNP superlattices at a lower magnification. The scale bar is 100 nm. See Video S6 for the full movie. The inset shows the corresponding FFT image which matches the diffraction pattern of a BCC crystal with the [210] zone axis. The scale bar is 0.1 nm^{-1}. (d) Effect of water radiolysis on graphene probed using Raman spectroscopy. Normalized Raman spectra (background-subtracted) of graphene before irradiation (black curve), graphene irradiated with water (red curve), and graphene irradiated without water (blue curve) are shown.

charged nature of DNA-AuNPs, which are in phosphate-buffered saline solution of pH 8, may be preventing their attachment to the silicon nitride windows and thus making their detection infrequent. Of those that were found, we observed dissociation immediately upon electron beam illumination (Figure 2b and Video S3). AuNPs were then seen to aggregate randomly at the silicon nitride window and etch over time (Figure 2c and Video S4). From these observations, we conclude that the DNA linkages are rapidly damaged, most likely as a result of hydroxyl radical attack, thereby causing the AuNPs to dissociate from the assembled structure and diffuse into the surrounding solution. The motion of individual AuNPs as they diffuse away is presumably too fast to be tracked with the time resolution of our camera as they are not slowed down by strong attachment to the silicon nitride windows. Random aggregation of AuNPs can be explained by the loss of electrostatic stabilization, previously imparted by the dense packing of negatively charged oligonucleotides, leading to decreased colloidal stability. The formation of close-packed aggregates lacking both long-range order and the expected interparticle spacing indicates that oligonucleotides are either no longer present at the surfaces of these AuNPs or severely damaged. Etching of aggregated AuNPs is attributed to oxidative dissolution caused by the hydroxyl radicals.[36]

To confirm the importance of graphene in providing protection against radiation damage in DNA-AuNP super-lattices, a graphene surface was integrated with the silicon nitride liquid cell design (Figure 3a). Silicon nitride windows were coated with graphene using the PMMA-mediated transfer method[37,38] and characterized using Raman spectroscopy. Similar to the silicon nitride liquid cell setup, DNA-AuNP superlattices are encapsulated between two microchips, but now with graphene surfaces in contact with the solution. Employing graphene-coated silicon nitride liquid cells, we were able to observe DNA-AuNP superlattices with long-range order

(Figures 3b and c, Videos S5 and S6), indicating that DNA linkages are structurally stable during imaging in the time scale of several minutes. The measured lattice spacing indicated in Figure 3b is 16.3 nm, which is close to the expected value of 16.6 nm for the {200} planes, and the FFT image shown in the inset of Figure 3c corresponds to the diffraction pattern of a BCC crystal with the [210] zone axis. DNA-AuNP superlattices appeared to be strongly attached to the windows, which could be due to binding of DNA to graphene driven by hydrophobic and $\pi-\pi$ stacking interactions.[39] Dissociation, aggregation, and etching of DNA-AuNP superlattices that were seen in silicon nitride liquid cells were not observed despite the use of similar imaging conditions. These results point toward specific properties of graphene as being responsible for the observed differences in DNA stability under irradiation.

When using graphene-coated silicon nitride liquid cells, bubbles appeared to form at the liquid–window interface as inferred from the observation that bubbles and AuNPs were in the same focal plane. As in previous graphene liquid cell experiments, bubble formation resulted in disordering of DNA-AuNP superlattices, but disordered DNA-AuNP assemblies remained stable against dissociation, aggregation, and etching which suggests that disordering was caused by mechanical forces of bubble-induced convection rather than radiation damage. Observation of bubble formation was surprising in itself since, at similar imaging conditions, it was not observed in silicon nitride liquid cells unless the electron beam intensity was drastically increased. Bubble formation in liquid-phase TEM has been attributed to the evolution of hydrogen gas as a byproduct of water radiolysis.[36] However, our qualitative observation suggests that graphene seems to be directly reacting with the products of water radiolysis, contrary to the assumption that it acts as a chemically inert window material.[19,21,40] To assess the changes to graphene that occur during liquid-phase TEM imaging, we carried out a correlative
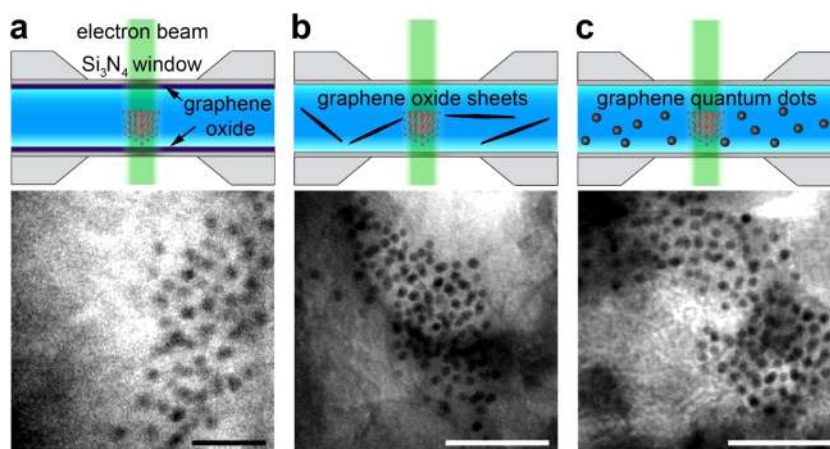
Figure 4. Imaging of DNA-AuNP assemblies using silicon nitride liquid cells with graphene oxide and graphene quantum dots as radical scavengers. (a) Graphene oxide sheets drop-casted onto the silicon nitride windows. The scale bar is 50 nm. See Video S7 for the full movie. (b) Graphene oxide sheets added to the solution. The scale bar is 100 nm. See Video S8 for the full movie. (c) Graphene quantum dots added to the solution. The scale bar is 100 nm. See Video S9 for the full movie.

Raman spectroscopy and liquid phase TEM study of graphene before and after imaging in water. If graphene is reacting with the water radiolysis products, we would expect to see an increase in the relative intensity of the D peak with respect to the G peak due to the formation of structural defects.[41] Additionally, the 2D peak is expected to broaden and decrease in intensity as graphene becomes more amorphous.[42] An area of 20 μm × 20 μm in the graphene-coated silicon nitride window was analyzed with Raman spectroscopy before and after exposure to a controlled electron beam dose in water (see Supporting Information). We carried out a control experiment by exposing graphene in another region of the same silicon nitride window to identical imaging conditions but in the dry state to assess the severity of knock-on damage in the absence of any water radiolysis products.[11] Raman spectra in Figure 3d show that the changes in relative intensities of D, G, and 2D peaks are greater when graphene is irradiated in water, confirming that graphene is reacting with the products of water radiolysis. Delamination of graphene in regions that were irradiated in water was also observed with TEM and optical microscopy.

The leading hypothesis to explain graphene's ability to reduce radiation damage in liquid-phase TEM has cited its excellent electrical and thermal properties.[20−22,24] But it has already been shown that electron beam-induced heating of the specimen is negligible in liquid cells where heat can be dissipated to the surrounding liquid,[36,43] so thermal conductivity does not appear to play a significant role. Electrostatic charging of the specimen and the windows by the ionizing electron beam[44] has been observed in previous silicon nitride liquid cell TEM studies.[45,46] Although it is plausible that electrically conducting graphene may help reduce electrostatic charging effects, it is unclear how electrical conductivity will counteract the detrimental effects of reactive radical species that form in solution. Our correlative Raman spectroscopy and TEM study suggests that we can no longer regard graphene as a chemically inert material that simply imparts electrical conductivity to the silicon nitride window. A more likely explanation is that graphene is acting as a radical scavenger. It has already been shown that isopropanol and ascorbic acid, which are effective radical scavengers, can be added to mitigate electron beam-induced galvanic replacement of AgNPs[47] and

oxidative dissolution of Au nanorods,[48] respectively. Recent electron spin resonance spectroscopy and spectrophotometric studies have demonstrated that graphene, graphene oxide, and graphene quantum dots are efficient hydroxyl radical scavengers.[49−52] It has been proposed that hydroxyl radicals react with graphene-based nanomaterials via electrophilic addition to conjugated C=C π-bonds or further oxidation of existing oxygen-containing functionalities.[49−51] Previous investigations of DNA stability against radiation damage in the presence of radical scavengers have shown that yields of DNA single-strand and double-strand breaks decreased as the radical scavenger concentration was increased.[53−55] Thus, an alternative hypothesis for the observed stability of biological specimens in graphene and graphene-coated silicon nitride liquid cells is that the graphene surfaces are scavenging radicals from water radiolysis, thereby protecting adjacent DNA-AuNP superlattices. Bubble formation observed when graphene is imaged in water at low electron beam intensities is presumably due to evolution of gases that are the byproducts of graphene oxidation.

If radical scavenging is the protection mechanism of graphene, then the protective effect should also be seen when radical scavenging graphene derivatives are present at the windows or in the solution. Consequently, we set out to image DNA-AuNP superlattices using silicon nitride liquid cells with graphene oxide and graphene quantum dots, which are being explored for biosensing and biomedical applications,[39,56] as biocompatible radical scavengers. The three liquid cell configurations that we used were as follows: graphene oxide sheets drop-casted onto silicon nitride windows (Figure 4a), graphene oxide sheets added to the solution (Figure 4b), and graphene quantum dots added to the solution (Figure 4c). In all three cases, DNA-AuNP assemblies were stable against dissociation, aggregation, and etching. Since graphene oxide is an insulator,[57] we can rule out the role of electrical conductivity. However, as noted previously with graphene and graphene-coated silicon nitride liquid cells, DNA-AuNP assemblies appear to be disordered by bubble formation. The greater amount of disordering observed in silicon nitride liquid cells with graphene-based radical scavengers compared to graphene liquid cells could be due to the greater volume of liquid being present, which would result in the creation of more

hydroxyl radicals that can react and cause bubble formation. Although liquid thicknesses were not directly measured for graphene and silicon nitride liquid cells, we can make the following estimations. Since the DNA-AuNPs within a given pocket exhibited limited range of motion, the vertical dimensions of pockets in graphene liquid cells appeared to be similar to the heights of encapsulated DNA-AuNP superlattices that were imaged (typically around 100 nm based on the number of unit cells). For silicon nitride liquid cells, the lower bound is defined by the height of the 150 nm spacer used. However, bending of the windows in high vacuum conditions can produce an actual height as large as 1 μm; any thicknesses greater than this would constrain our imaging capability. It is also possible that the small dimensions of the pockets present in graphene liquid cells could be exerting confinement effects on the DNA-AuNP superlattices, thereby restricting their movement and so minimizing the disordering. Use of multilayer (3−5 layers) rather than single/double layer graphene as the window material allowed encapsulation of more liquid[24] but led to more vigorous bubble formation and thus faster disordering of DNA-AuNP superlattices. Regardless, we conclude that radical scavenging ability is the crucial parameter that explains the enhanced protection of the specimen against radiation damage in the graphene liquid cell compared to its silicon nitride counterpart.

In this work, we show that graphene and its derivatives can be used as biocompatible radical scavengers to mitigate radiation damage, which currently represents a bottleneck preventing the application of liquid-phase TEM as a popular method for studying radiation-sensitive biological specimens. Based on our study, we advocate the use of graphene liquid cells as they offer optimal image contrast and spatial resolution for a given electron dose, while the chemical properties of graphene provide protection against radiation damage. By adding water-soluble graphene derivatives directly to the solution, it may be possible to reduce radiation damage even further, which could also lead to prolonged lifetime of the liquid pockets by retarding the formation of defects in the graphene windows. For graphene-coated silicon nitride liquid cells, the hydrophobicity of the window surfaces meant that microchips were often incompletely wetted, causing regions of the liquid cell to be dried out. Thus, when using silicon nitride liquid cells, we recommend that hydrophilic graphene derivatives should be used both as additives to the solution and as coatings on the windows. Although the scope of this study has focused on the use of graphene and its derivatives, it is likely that alternative radical scavengers could produce a similar protective effect. Further investigation is needed to determine the most effective radical scavenger that should be used in future liquid-phase TEM studies where minimal perturbation by the electron beam is desired. Ideally, unsupported graphene windows should be integrated with the existing microchip-based liquid cell platform to combine the advantages of graphene liquid cells with technical capabilities that facilitate liquid flow, heating, and electrical biasing. This would enable characterization capabilities that complement X-ray crystallography, solution nuclear magnetic resonance spectroscopy, cryo-electron microscopy, and super-resolution fluorescence microscopy.

■ ASSOCIATED CONTENT

ⓢ Supporting Information

The Supporting Information is available free of charge on the ACS Publications website at DOI: 10.1021/acs.nanolett.6b04383.

> Experimental details and Figures S1−S3 (PDF)
> Video S1: Disordering of DNA-AuNP superlattices encapsulated in a graphene liquid cell via bubble generation in the surrounding aqueous solution at high electron beam intensities (AVI)
> Video S2: Disordering of DNA-AuNP superlattices (different from those shown in Video S1) encapsulated in a graphene liquid cell via bubble generation in the surrounding aqueous solution at high electron beam intensities (AVI)
> Video S3: Dissociation of DNA-AuNP superlattices inside a silicon nitride liquid cell resulting from DNA damage under electron beam irradiation (AVI)
> Video S4: Aggregation of destabilized AuNPs inside a silicon nitride liquid cell (AVI)
> Video S5: DNA-AuNP superlattices imaged using a graphene-coated silicon nitride liquid cell (AVI)
> Video S6: DNA-AuNP imaged at a lower magnification using a graphene-coated silicon nitride liquid cell (AVI)
> Video S7: Stable DNA-AuNP assemblies imaged using a graphene oxide-coated silicon nitride liquid cell (AVI)
> Video S8: Stable DNA-AuNP assemblies imaged using a silicon nitride liquid cell with graphene oxide sheets added to the solution (AVI)
> Video S9: Stable DNA-AuNP assemblies imaged using a silicon nitride liquid cell with graphene quantum dots added to the solution (AVI)

■ AUTHOR INFORMATION

Corresponding Author
*E-mail: paul.alivisatos@berkeley.edu.

ORCID ⓘ
Hoduk Cho: 0000-0002-0082-0637
A. Paul Alivisatos: 0000-0001-6895-9048

Notes
The authors declare no competing financial interest.

■ REFERENCES

(1) Williamson, M. J.; Tromp, R. M.; Vereecken, P. M.; Hull, R.; Ross, F. M. *Nat. Mater.* **2003**, *2*, 532−536.
(2) Ross, F. M. *Science* **2015**, *350*, aaa9886.
(3) de Jonge, N.; Peckys, D. B.; Kremers, G. J.; Piston, D. W. *Proc. Natl. Acad. Sci. U. S. A.* **2009**, *106*, 2159−2164.
(4) Peckys, D. B.; de Jonge, N. *Nano Lett.* **2011**, *11*, 1733−1738.

(5) Pohlmann, E. S.; Patel, K.; Guo, S.; Dukes, M. J.; Sheng, Z.; Kelly, D. F. *Nano Lett.* **2015**, *15*, 2329−2335.

(6) Hermannsdörfer, J.; Tinnemann, V.; Peckys, D. B.; de Jonge, N. *Microsc. Microanal.* **2016**, *22*, 656−665.

(7) de Jonge, N.; Ross, F. M. *Nat. Nanotechnol.* **2011**, *6*, 695−704.

(8) Mirsaidov, U. M.; Zheng, H.; Casana, Y.; Matsudaira, P. *Biophys. J.* **2012**, *102*, L15−7.

(9) Peckys, D. B.; de Jonge, N. *Microsc. Microanal.* **2014**, *20*, 1−20.

(10) Woehl, T. J.; Kashyap, S.; Firlar, E.; Perez-Gonzalez, T.; Faivre, D.; Trubitsyn, D.; Bazylinski, D. A.; Prozorov, T. *Sci. Rep.* **2014**, *4*, 6854.

(11) Egerton, R. F.; Li, P.; Malac, M. *Micron* **2004**, *35*, 399−409.

(12) von Sonntag, C. *Free-Radical-Induced DNA Damage and Its Repair*; Springer: Berlin, Germany, 2006.

(13) Hutchinson, F. *Prog. Nucleic Acid Res. Mol. Biol.* **1985**, *32*, 115−154.

(14) Breen, A. P.; Murphy, J. A. *Free Radical Biol. Med.* **1995**, *18*, 1033−1077.

(15) Balasubramanian, B.; Pogozelski, W. K.; Tullius, T. D. *Proc. Natl. Acad. Sci. U. S. A.* **1998**, *95*, 9738−9743.

(16) Burrows, C. J.; Muller, J. G. *Chem. Rev.* **1998**, *98*, 1109−1152.

(17) Ward, J. F. *Prog. Nucleic Acid Res. Mol. Biol.* **1988**, *35*, 95−125.

(18) Pogozelski, W. K.; Tullius, T. D. *Chem. Rev.* **1998**, *98*, 1089−1108.

(19) Yuk, J. M.; Park, J.; Ercius, P.; Kim, K.; Hellebusch, D. J.; Crommie, M. F.; Lee, J. Y.; Zettl, A.; Alivisatos, A. P. *Science* **2012**, *336*, 61−64.

(20) Mohanty, N.; Fahrenholtz, M.; Nagaraja, A.; Boyle, D.; Berry, V. *Nano Lett.* **2011**, *11*, 1270−1275.

(21) Chen, Q.; Smith, J. M.; Park, J.; Kim, K.; Ho, D.; Rasool, H. I.; Zettl, A.; Alivisatos, A. P. *Nano Lett.* **2013**, *13*, 4556−4561.

(22) Chen, Q.; Smith, J. M.; Rasool, H. I.; Zettl, A.; Alivisatos, A. P. *Faraday Discuss.* **2015**, *175*, 203−214.

(23) Wang, C.; Qiao, Q.; Shokuhfar, T.; Klie, R. F. *Adv. Mater.* **2014**, *26*, 3410−3414.

(24) Park, J.; Park, H.; Ercius, P.; Pegoraro, A. F.; Xu, C.; Kim, J. W.; Han, S. H.; Weitz, D. A. *Nano Lett.* **2015**, *15*, 4737−4744.

(25) Nair, R. R.; Blake, P.; Blake, J. R.; Zan, R.; Anissimova, S.; Bangert, U.; Golovanov, A. P.; Morozov, S. V.; Geim, A. K.; Novoselov, K. S.; Latychevskaia, T. *Appl. Phys. Lett.* **2010**, *97*, 153102.

(26) Zan, R.; Ramasse, Q. M.; Jalil, R.; Georgiou, T.; Bangert, U.; Novoselov, K. S. *ACS Nano* **2013**, *7*, 10167−10174.

(27) Algara-Siller, G.; Kurasch, S.; Sedighi, M.; Lehtinen, O.; Kaiser, U. *Appl. Phys. Lett.* **2013**, *103*, 7−12.

(28) Park, S. Y.; Lytton-Jean, A. K. R.; Lee, B.; Weigand, S.; Schatz, G. C.; Mirkin, C. A. *Nature* **2008**, *451*, 553−556.

(29) Nykypanchuk, D.; Maye, M. M.; van der Lelie, D.; Gang, O. *Nature* **2008**, *451*, 549−552.

(30) Jones, M. R.; Seeman, N. C.; Mirkin, C. A. *Science* **2015**, *347*, 1260901.

(31) Kewalramani, S.; Guerrero-García, G. I.; Moreau, L. M.; Zwanikken, J. W.; Mirkin, C. A.; Olivera de la Cruz, M. O.; Bedzyk, M. J. *ACS Cent. Sci.* **2016**, *2*, 219−224.

(32) Bishop, K. J. M.; Wilmer, C. E.; Soh, S.; Grzybowski, B. A. *Small* **2009**, *5*, 1600−1630.

(33) Noll, D. M.; Mason, T. M.; Miller, P. S. *Chem. Rev.* **2006**, *106*, 277−301.

(34) Deans, A. J.; West, S. C. *Nat. Rev. Cancer* **2011**, *11*, 467−480.

(35) Chee, S. W.; Baraissov, Z.; Loh, N. D.; Matsudaira, P. T.; Mirsaidov, U. *J. Phys. Chem. C* **2016**, *120*, 20462−20470.

(36) Schneider, N. M.; Norton, M. M.; Mendel, B. J.; Grogan, J. M.; Ross, F. M.; Bau, H. H. *J. Phys. Chem. C* **2014**, *118*, 22373−22382.

(37) Reina, A.; Son, H.; Jiao, L.; Fan, B.; Dresselhaus, M. S.; Liu, Z.; Kong, J. *J. Phys. Chem. C* **2008**, *112*, 17741−17744.

(38) Li, X.; Cai, W.; An, J.; Kim, S.; Nah, J.; Yang, D.; Piner, R.; Velamakanni, A.; Jung, I.; Tutuc, E.; Banerjee, S. K.; Colombo, L.; Ruoff, R. S. *Science* **2009**, *324*, 1312−1314.

(39) Tang, L.; Wang, Y.; Li, J. *Chem. Soc. Rev.* **2015**, *44*, 6954−6980.

(40) Yuk, J. M.; Zhou, Q.; Chang, J.; Ercius, P.; Alivisatos, A. P.; Zettl, A. *ACS Nano* **2016**, *10*, 88−92.

(41) Ferrari, A. C.; Basko, D. M. *Nat. Nanotechnol.* **2013**, *8*, 235−246.

(42) Ferrari, A. C. *Solid State Commun.* **2007**, *143*, 47−57.

(43) Zheng, H.; Claridge, S. A.; Minor, A. M.; Alivisatos, A. P.; Dahmen, U. *Nano Lett.* **2009**, *9*, 2460−2465.

(44) Cazaux, J. *Ultramicroscopy* **1995**, *60*, 411−425.

(45) Woehl, T. J.; Jungjohann, K. L.; Evans, J. E.; Arslan, I.; Ristenpart, W. D.; Browning, N. D. *Ultramicroscopy* **2013**, *127*, 53−63.

(46) White, E. R.; Mecklenburg, M.; Shevitski, B.; Singer, S. B.; Regan, B. C. *Langmuir* **2012**, *28*, 3695−3698.

(47) Sutter, E.; Jungjohann, K.; Bliznakov, S.; Courty, A.; Maisonhaute, E.; Tenney, S.; Sutter, P. *Nat. Commun.* **2014**, *5*, 4946.

(48) Chen, Q.; Cho, H.; Manthiram, K.; Yoshida, M.; Ye, X.; Alivisatos, A. P. *ACS Cent. Sci.* **2015**, *1*, 33−39.

(49) Qiu, Y.; Wang, Z.; Owens, A. C. E.; Kulaots, I.; Chen, Y.; Kane, A. B.; Hurt, R. H. *Nanoscale* **2014**, *6*, 11744−11755.

(50) Radich, J. G.; Kamat, P. V. *ACS Nano* **2013**, *7*, 5546−5557.

(51) Yu, C.; Zhang, B.; Yan, F.; Zhao, J.; Li, J.; Li, L.; Li, J. *Carbon* **2016**, *105*, 291−296.

(52) Chong, Y.; Ge, C.; Fang, G.; Tian, X.; Ma, X.; Wen, T.; Wamer, W. G.; Chen, C.; Chai, Z.; Yin, J. J. *ACS Nano* **2016**, *10*, 8690−8699.

(53) Ward, J. F.; Blakely, W. F.; Joner, E. I. *Radiat. Res.* **1985**, *103*, 383−392.

(54) Siddiqi, M. A.; Bothe, E. *Radiat. Res.* **1987**, *112*, 449−463.

(55) Krisch, R. E.; Flick, M. B.; Trumbore, C. N. *Radiat. Res.* **1991**, *126*, 251−259.

(56) Loh, K. P.; Bao, Q.; Eda, G.; Chhowalla, M. *Nat. Chem.* **2010**, *2*, 1015−1024.

(57) Lim, S. Y.; Shen, W.; Gao, Z. *Chem. Soc. Rev.* **2015**, *44*, 362−381.